A Ffowcs Williams – Hawkings Solver for Lattice-Boltzmann Based Computational Aeroacoustics

3 authors:

Guillaume Brès
Cascade Technologies
86 PUBLICATIONS   **3,921** CITATIONS

SEE PROFILE

David Freed
OnScale
51 PUBLICATIONS   **1,041** CITATIONS

SEE PROFILE

Franck Perot
Altair Engineering
58 PUBLICATIONS   **1,285** CITATIONS

SEE PROFILE

A Ffowcs Williams–Hawkings Solver for Lattice-Boltzmann based Computational Aeroacoustics

Guillaume A. Brès[*], Franck Pérot[†], and David Freed[‡]

Exa Corporation, Brisbane, CA 94005, U.S.A.

This paper presents the development of an efficient far-field noise prediction code using the near-field results from a Lattice-Boltzmann flow solver as input to an acoustic analogy solver. Two formulations, based on the Ffowcs Williams–Hawkings equation, are implemented to efficiently perform far-field prediction from large input data sets. For configuration where the noise source is moving through a fluid at rest (such as aircraft certification), the efficient and well-validated formulation 1A is implemented. For wind-tunnel configurations where both the source and observer are stationary in a uniform flow, a formulation based on the Garrick Triangle, and referred to as GT, is used to increase the computational efficiency. Numerical simulations and far-field prediction are performed for three representative validation cases: a three-dimensional monopole source, a tandem cylinder flow, and a fan noise case. Comparisons of the results from the far-field solver show excellent agreement with the theoretical predictions and the available experimental data.

Nomenclature

c	Speed of sound
$f = 0$	Integration surface definition
g	Retarded-time variable
H	Heaviside function
$\mathbf{M}$	Mach number vector of the source
M_0	Wind-tunnel Mach number
$\hat{\mathbf{n}}$	Local unit normal vector to the surface
P_{ij}	Compressible stress tensor
p	Pressure
R	Garrick triangle distance
Re	Reynolds number
r	Distance between observer and source
$\hat{\mathbf{r}}$	Unit vector in the radiation direction
t	Observer (reception) time
$\mathbf{U_0}$	Wind-tunnel velocity
$\mathbf{u}$	Fluid velocity
$\mathbf{v}$	Surface velocity
$\mathbf{x}$	Observer position

$\mathbf{y}$	Source position
β	$\sqrt{1 - M_0^2}$
δ	Dirac function
ρ	Density
τ	Source (emission) time

Subscript

0	Ambient quantity
i, j	Vector component in fixed reference frame
n	Projection in the normal direction
r	Projection in the radiation direction
ret	Quantity evaluated at the retarded time

Superscript

$*$	Wind-tunnel quantity
$'$	Disturbance quantity (e.g., $\rho' = \rho - \rho_0$)
$\cdot$	Source-time derivative
$\hat{}$	Unit vector

I.   Introduction

For practical applications such as aircraft or train certification, prediction of the far-field noise with numerical simulations remains challenging, despite recent progress in computational aeroacoustics (CAA). Such engineering problems involve large distances, making it impractical to accurately resolve the propagation

---

[*]Principal Aeroacoustics Engineer, Senior Member AIAA
[†]Manager Aeroacoustics applications, Member AIAA
[‡]Senior Director of Aeroacoustics Applications

American Institute of Aeronautics and Astronautics

of the small amplitude acoustic fluctuations from the near-field source region to the far-field microphones within the computational domain.

A classical approach to overcome this difficulty is through the use of integral methods: first, computational fluid dynamic (CFD) simulations are performed to capture all the potential noise sources in the near-field (i.e., sound generation mechanism); then an acoustic analogy method is used to propagate this near-field information to the far-field (i.e., sound propagation mechanism). This paper presents the development and implementation of an efficient far-field noise prediction code relying on Lattice Boltzmann method (LBM) for the CFD simulation, and on the Ffowcs Williams–Hawkings (FW-H) equation[1] for the acoustic analogy method.

The CFD/CAA code PowerFLOW 4.2 based on the Lattice Boltzmann method is used in this study. LBM simulations have been used extensively for aerodynamics and flow prediction over a wide range of problems, from simplified geometries[2,3] to fully detailed ground vehicles[4,5] and aerospace applications.[6,7] Coupled with turbulence modeling, the LBM scheme has been shown to accurately resolve the large-scale unsteady flow structures and the turbulent wall pressure fluctuations due to separated and reattached flows.[8,9] These structures and pressure disturbances are key components of the near-field sound sources, which, through the acoustic analogy method, will be the main contributors to the far-field noise. Details of the LBM code, including the fundamental Lattice Boltzmann equations, numerical scheme, wall boundary conditions, and turbulence modeling, can be found in Refs. 10–13.

For real-world applications such as landing gear noise and train certification, the CFD input to the acoustic analogy method is expected to be large, requiring numerically efficient methods for the far-field noise prediction capability. The implemented FW-H solver was developed to efficiently handle these large data sets for arbitrary moving noise sources, both in a fluid at rest (e.g., aircraft fly-over or train pass-by configuration) and in a uniform flow (e.g., wind-tunnel testing or wind-turbine noise). For the former case (referred to as *moving-source*), the time-domain FW-H formulation developed by Farassat known as formulation 1A[14,15] is an efficient and concise method well-suited for numerical computation. For the most general form of the latter case, an extension of Formulation 1A based on the convective form of FW-H equation was developed to predict far-field sound radiation of an arbitrary moving source in uniformly moving media.[16] In the present work, only the typical wind-tunnel testing is considered, where both the source and observer are stationary in a uniform flow. For this particular case (referred to as *wind-tunnel*), a formulation based on the Garrick Triangle[17,18] is used to increase the computational efficiency.

Details on the different formulations and the numerical implementation are presented in section II. Validation of the coupling between the CFD and the acoustic analogy method is shown for a three-dimensional monopole source in section III. Results for tandem cylinder noise (representative of the *wind-tunnel* capability) are then presented in section IV, including comparison with the measured radiated noise from experiments. Finally, preliminary results for fan noise (representative of the *moving-source* capability) are discussed in section V.

II.   Acoustic analogy method

A.   Ffowcs Williams–Hawkings equation

The starting point is the Ffowcs Williams–Hawkings (FW-H) equation[1] for a porous (permeable) surface, written in differential form as

$$\Box^2 c^2(\rho - \rho_0) = \frac{\partial}{\partial t}\left[Q_n \delta(f)\right] - \frac{\partial}{\partial x_i}\left[L_i \delta(f)\right] + \frac{\partial}{\partial x_i \partial x_j}\left[T_{ij} H(f)\right], \tag{1}$$

where the variables Q_n and L_i are defined as

$$Q_n = Q_i \hat{n}_i = \left[\rho_0 v_i + \rho(u_i - v_i)\right]\hat{n}_i, \tag{2}$$

$$L_i = L_{ij}\hat{n}_j = \left[P_{ij} + \rho u_i(u_j - v_j)\right]\hat{n}_j. \tag{3}$$

The wave operator is $\Box^2 = 1/c^2 \partial^2/\partial t^2 - \nabla^2$. These equations are an exact rearrangement of the continuity and Navier–Stokes equations. The moving data surface is typically described by $f(\mathbf{x}, t) = 0$ such that $\hat{\mathbf{n}} = \nabla f$ is the unit outward normal to the surface. Here v_i are the velocities of the surface f, u_i are the fluid velocities on f, and the summation convention is used for repeated index. This porous (permeable)

American Institute of Aeronautics and Astronautics

data surface formulation allows for the nonlinearities in the vicinity of the solid surface to be taken into account (i.e., the acoustic sources in the flow field outside the solid surface but inside the data surface). If $f = 0$ correspond to the solid surface, then $u_i = v_i$, and the original FW-H equation for solid (impenetrable) surface is retrieved.

The first two terms in the right-hand side of equation (1) correspond to surface integrals and are typically referred to as thickness source (or monopole) term and loading source (or dipole) term. The last term, the volume integral, is the quadrupole source term, which is typically small compared to the other contributions. This term is also more challenging to compute and is often neglected.

A few assumptions are then introduced. In equations (1) and (3), the Lighthill stress tensor and the compressible stress tensor are defined as $T_{ij} = \rho u_i u_j + P_{ij} + c^2(\rho - \rho_0)\delta_{ij}$, and $P_{ij} = (p - p_0)\delta_{ij} - \tau_{ij}$, respectively, where σ_{ij} is the viscous stress tensor and δ_{ij} is the Kronecker delta. In general, the viscous term in P_{ij} is a negligible source of sound and is typically neglected, i.e., $P_{ij} = (p - p_0)\delta_{ij}$[a]. Also, outside of the source region, density perturbations are expected to be small, so the term $c^2(\rho - \rho_0)$ is replaced by the acoustic pressure p' to obtain an inhomogeneous wave equation.

B. Far-field noise prediction in moving-source configuration: formulation 1A

Farassat's formulation 1A[14, 15] is implemented to predict the noise generated by an acoustic source moving in a fluid at rest, and measured at a stationary observer located in the far-field. This formulation is computationally efficient and has been widely used, especially for the prediction of rotor and propeller noise.[20]

Neglecting the quadrupole terms, the acoustic pressure p' generated by a source in subsonic motion at the observer position $\mathbf{x}$ and observer time t is given by the following integral solution of equation (1):

$$p'(\mathbf{x}, t) = p'_T(\mathbf{x}, t) + p'_L(\mathbf{x}, t), \tag{4}$$

where the subscript T and L correspond to the thickness and loading components, defined respectively as

$$
\begin{aligned}
4\pi p'_T(\mathbf{x}, t) = &\int_{f=0} \left[\frac{\dot{Q}_n + Q_{\dot{n}}}{r(1 - M_r)^2}\right]_{ret} dS \\
&+ \int_{f=0} \left[\frac{Q_n(r\dot{M}_r + c_0(M_r - M^2))}{r^2(1 - M_r)^3}\right]_{ret} dS,
\end{aligned} \tag{5}
$$

$$
\begin{aligned}
4\pi p'_L(\mathbf{x}, t) = &\frac{1}{c_0}\int_{f=0} \left[\frac{\dot{L}_r}{r(1 - M_r)^2}\right]_{ret} dS \\
&+ \int_{f=0} \left[\frac{L_r - L_M}{r^2(1 - M_r)^2}\right]_{ret} dS \\
&+ \frac{1}{c_0}\int_{f=0} \left[\frac{L_r(r\dot{M}_r + c_0(M_r - M^2))}{r^2(1 - M_r)^3}\right]_{ret} dS.
\end{aligned} \tag{6}
$$

Here, $\mathbf{M}$ is the Mach number vector of the source, with component $M_i = v_i/c_0$, and the superscript $\dot{}$ denotes derivative with respect to the source time τ. Therefore, the remaining terms are explicitly defined as

$$M_r = M_i \hat{r}_i, \qquad \dot{M}_r = \frac{\partial M_i}{\partial \tau}\hat{r}_i, \tag{7}$$

$$Q_n = Q_i \hat{n}_i, \qquad \dot{Q}_n = \frac{\partial Q_i}{\partial \tau}\hat{n}_i, \qquad Q_{\dot{n}} = Q_i \frac{\partial \hat{n}_i}{\partial \tau}, \tag{8}$$

$$L_i = L_{ij}\hat{n}_i, \qquad \dot{L}_r = \frac{\partial L_i}{\partial \tau}\hat{r}_i, \qquad L_r = L_i \hat{r}_i, \qquad L_M = L_i M_i. \tag{9}$$

---

[a]Ffowcs Williams and Hawkings,[1] as well as Farassat,[19] use the notation p instead of $p - p_0$ to denote the gauge pressure. Brentner[20] suggested the notation P_{ij} to avoid confusion.

The subscript *ret* denotes the evaluation of the integrand at the time of emission, i.e., the solution τ_{ret} of the retarded-time equation

$$g = \tau_{ret} - t + \frac{r}{c_0} = 0. \tag{10}$$

where $r = |\mathbf{x} - \mathbf{y}(\tau_{ret})|$ is the distance between observer and source at the time of emission.

C. Wind-tunnel configuration: formulation GT

In the particular *wind-tunnel* case where both the source and observer are stationary in the uniform flow, simplifications in the formulation lead to increase in computational efficiency. Without loss of generality, it can be assumed that the mean flow velocity is in the $+x_1$ direction[b], i.e., $\mathbf{U_0} = (U_{01}, 0, 0)$. This problem of a fixed source (and fixed observer) in a uniform flow is equivalent to a source (and observer) moving with speed $-\mathbf{U_0}$ in a fluid at rest, and can therefore be expressed as a special form of formulation 1A.

For a source in uniform rectilinear subsonic motion, the retarded-time equation in equation (10) has a unique solution given by the Garrick Triangle:[17]

$$\tau_{ret} = t - \frac{R}{c_0}, \tag{11}$$

where the distance R is now defined as

$$R = \frac{-M_0(x_1 - y_1) + R^*}{\beta^2}, \tag{12}$$

with

$$R^* = \sqrt{(x_1 - y_1)^2 + \beta^2[(x_2 - y_2)^2 + (x_3 - y_3)^2]}, \tag{13}$$

and

$$\beta = \sqrt{1 - M_0^2}. \tag{14}$$

Here, R represents the effective *acoustic* distance (rather than the geometric distance) between the source and the observer in terms of time delay between emission and reception.[21] The unit radiation vector components $\hat{R}_i = (\nabla R)_i / |\nabla R|$ and M_R are now defined by

$$\hat{R}_1 = \frac{-M_0 R^* + (x_1 - y_1)}{\beta^2 R}, \qquad \hat{R}_2 = \frac{x_2 - y_2}{R}, \qquad \hat{R}_3 = \frac{x_3 - y_3}{R}, \qquad M_R = M_i \hat{R}_i \tag{15}$$

The definitions of Q_n and L_i are identical to equations (2) and (3), where the surface velocities v_i have been replaced by $-U_{0i}$, since all the velocities need to be expressed in the stationary frame of the fluid at rest:

$$Q_n = [-\rho_0 U_{0i} + \rho(u_i + U_{0i})] \, \hat{n}_i, \tag{16}$$

$$L_i = [P_{ij} + \rho u_i(u_j + U_{0j})] \, \hat{n}_j. \tag{17}$$

Unlike the physical separation distance r in a general motion case, the distance R is constant, no longer a function of time. The same holds for $\hat{R}_i$ and M_R. Therefore, these variables can be evaluated and stored at the preprocessing step, rather than computed at every time step, and their source time derivative is zero. Likewise, because of the uniform rectilinear motion of the source, the source Mach number $\mathbf{M}$ and the normal vectors $\hat{n}$ are not a function of time, so $\dot{M}_R = 0$ and $\dot{\hat{n}} = 0$.

These simplifications lead to the following form of the formulation:

$$
\begin{aligned}
4\pi p'_T(\mathbf{x}, t) = & \int_{f=0} \left[\frac{\dot{Q}_n}{R(1 - M_R)^2} \right]_{ret} dS \\
& + \int_{f=0} \left[\frac{Q_n c_0(M_R - M^2)}{R^2(1 - M_R)^3} \right]_{ret} dS,
\end{aligned}
\tag{18}
$$

---

[b]Otherwise, the reference frame can be rotated to satisfy this condition

$$4\pi p'_Q(\mathbf{x},t) = \frac{1}{c_0} \int_{f=0} \left[\frac{\dot{L}_R}{R(1-M_R)^2} \right]_{ret} dS$$
$$+ \int_{f=0} \left[\frac{L_R - L_M}{R^2(1-M_R)^2} \right]_{ret} dS \tag{19}$$
$$+ \int_{f=0} \left[\frac{L_R(M_R - M^2)}{R^2(1-M_R)^3} \right]_{ret} dS,$$

Note that the subscript ret still denotes the evaluation of the integrand at the time of emission, which is now computed using equation (11).

The formulation using the Garrick Triangle (referred to as GT) is therefore similar to formulation 1A in equations (5) and (6), where the source time derivative of the constant terms $\mathbf{M}$ and $\hat{n}$ are not computed, and the terms r, M_r and $\hat{\mathbf{r}}$ have been replaced by R, M_R and $\hat{\mathbf{R}}$, respectively. An alternative and equivalent way to obtain the formulation GT is to derive it from the convective form of FW-H equation,[16] as shown in Ref. 22. In that case, the effective distance R is introduced by the use of the convective Green's function (rather than the traditional free-space Green's function). In the limit $M_0 = 0$ (e.g., a stationary monopole source in a fluid at rest, as discussed in section III), the distance $R = r$, and all the formulations are identical.

D. Numerical implementation

The input to the FW-H solver is the time-dependent flow field on a surface mesh, both provided by CFD simulations with the LBM code. The surface mesh elements (panels) are typically much smaller than any representative acoustic wavelength, and are therefore considered as compact sources for the acoustic analogy solver. The flow properties and the geometry information (i.e., panel coordinates, unit normal, area) are specified at the center of the panel, and directly loaded from the CFD simulation. Simple first-order method is used to perform the spatial integration over the surface. The source time derivation is performed using fourth-order central differences.

For the evaluation of the retarded-time equation in equations (10) and (11), two different methods are available: in the first approach, commonly referred to as retarded-time algorithm, the reception time t is fixed, and the retarded-time equation is solved for the root τ_{ret}, the time at which the sound reaching the observer at time t was emitted. In the general case, the source position is a function of time, $\mathbf{y} = \mathbf{y}(\tau_{ret})$, and iterative or root-finding methods are needed to find the solution of the retarded-time equation. This approach also requires the discrete transient input data to be interpolated at time τ_{ret}.

The second approach, referred to as source-time dominant algorithm[20,23] (or advanced time approach[24]), use the same formulation but inverts the role of τ and t: here, the emission time τ is chosen, and the retarded-time equation is solved for t, the time when the sound from the source $\mathbf{y}(\tau)$ will reach the observer. Here, the determination of the reception time t can be done analytically, assuming that the observers are stationary.

For the current work, the source-time dominant algorithm was implemented, as it is better suited to handle large sets of time-dependent CFD input. This approach has the advantage that the integrands are directly evaluated at the time at which the CFD input is available (i.e., no time interpolation of the input data required). Only one snapshot of the full transient CFD data set is loaded and manipulated at once. However, this sequence of equally spaced CFD input time (i.e., emission time) will lead to unequally spaced reception time: sound emitted at the same time by different panels on the surface will reach the observer at different times. Therefore, time interpolation of the output pressure time history is required for each individual panel, to ensure that the contributions from all the source panels are accounted for and summed at the same reception time t. The current procedure to reconstruct $p'(\mathbf{x},t)$ is essentially based on linear interpolation, and the sampling frequency of the acoustic pressure signal in output of the FW-H solver is identical to the input sampling frequency. More accurate schemes will be investigated in future work.

The computational and memory requirements are also decreased if the input data for the FW-H solver corresponds to the solid surface. In that case, $u_i = v_i$ and the equations (2) and (3) simplify to $Q_n = \rho_0 v_i \hat{n}_i$ and $L_i = (p - p_0)\delta_{ij}\hat{n}_j$, respectively. Additionally, for *wind-tunnel* cases using solid integration surfaces, Q_n is independent of time, and as a result, so is p'_T. Therefore the thickness source does not contribute to the noise in this case, and is not computed to save computational time.

American Institute of Aeronautics and Astronautics

While acoustic analogy calculations are typically very efficient compare to the CFD near-field simulations, the computational cost may become significant for predictions involving a large number of time samples, surface elements and/or observers. For practical landing gear noise prediction[25] for instance, the FW-H input surface can contain several millions of panels, and thousands of time frames, if that surface coincides with the physical detailed surface geometry (i.e., solid formulation). Fortunately, FW-H solvers are well suitable for parallelization, since the calculations at each observer and for each surface element are independent. While the code used in this work is a serial solver, parallel implementation using MPI is currently underway.

III.   Three-dimensional monopole noise source

The first validation case corresponds to the canonical problem of sound radiation by a three-dimensional monopole in a fluid at rest. Comparisons with analytical solutions are discussed in Refs. 16 and 22, for both stationary and moving monopole. Here, results are presented mainly to validate the coupling between the CFD from the LBM solver and the acoustic analogy method.

A.   Numerical setup

For the LBM simulation, the numerical scheme is solved on a grid composed of cubic volumetric elements called voxels, and variable resolution (VR) is allowed, where the grid size changes by a factor of two for adjacent resolution regions. The three-dimensional monopole source is characterized by harmonic fluctuations of pressure and velocity imposed as a time-dependent boundary condition on a small sphere centered at the origin. Here, the monopole frequency is $f = 1000$ Hz (wavelength $\lambda = f/c_0$), and the sphere radius is $r_0 = \lambda/8$ such that the source is considered compact. The monopole pressure amplitude at r_0 is initialized to P_0, and the simulation time is 100 periods.

The size of the computational domain is about 60λ in all directions. The zone of interest for the CFD near-field measurements is $0.5\lambda < r < 7\lambda$, where r is the distance from the source. In that region, the spatial resolution is uniform (i.e., the number of points per wavelength N_{ppw} is constant). The outer part of the domain $r > 7\lambda$ corresponds to a large acoustics buffer zone with coarser resolution, implemented to avoid any reflection and spurious waves.

For $r < 0.5\lambda$, resolution is increased to properly resolve the monopole source. Three VR transitions are introduced such that the number of points per source radius is identical to N_{ppw}. Additionally, the pressure amplitude and particle speed on the surface are defined such that an harmonic spherical wave is generated at $r = r_0$ (see Chap. 5 in Ref. 26 for details). While different setup were initially considered, the combination of these boundary conditions with the added local resolution ultimately yields the most accurate prediction for the source strength (i.e., the measured monopole amplitude in the LBM simulation matches P_0 with less than 1% error).

B.   Near-field and far-field results

Simulations with spatial resolution of $N_{ppw} = 8$, 12, 16 and 20 are performed. The transient pressure, density and velocities are recorded on a sphere of radius $r_0 + \lambda$ enclosing the monopole, and is used as input to the FW-H solver, with the porous surface formulation. The acoustic pressure field is computed at several microphone positions, both in the near-field and far-field.

For accurate FW-H prediction, the sampling frequency of the FW-H input surface needs to be sufficient to appropriately capture the main frequency of interest of the noise source. For each case considered here, the FW-H input surface sampling frequency was between 15 and 35 times the monopole frequency. By artificially reducing this sampling frequency, the threshold for good far-field prediction can be estimated at 10 to 12 time steps per period. Significant drop off is observed below 4 to 5 points per period.

Since some of the measurements are performed in relatively close proximity to the source, the pressure field can be calculated directly in the LBM simulation, provided that the grid resolution is sufficient. Based on previous study of the acoustic properties of the Lattice Boltzmann method,[27] a grid resolution of 12 points per wavelength (and above) is expected to lead to negligible numerical losses. The acoustic pressure field is therefore directly recorded every λ in the zone of interest. The comparison of the FW-H results for the different spatial resolution shows that the choice of 12 to 16 points per wavelength was sufficient to accurately capture the near-field fluctuations. Even for the simulation with $N_{ppw} = 8$, the deviation of the RMS pressure from the theoretical value is only about 5%.
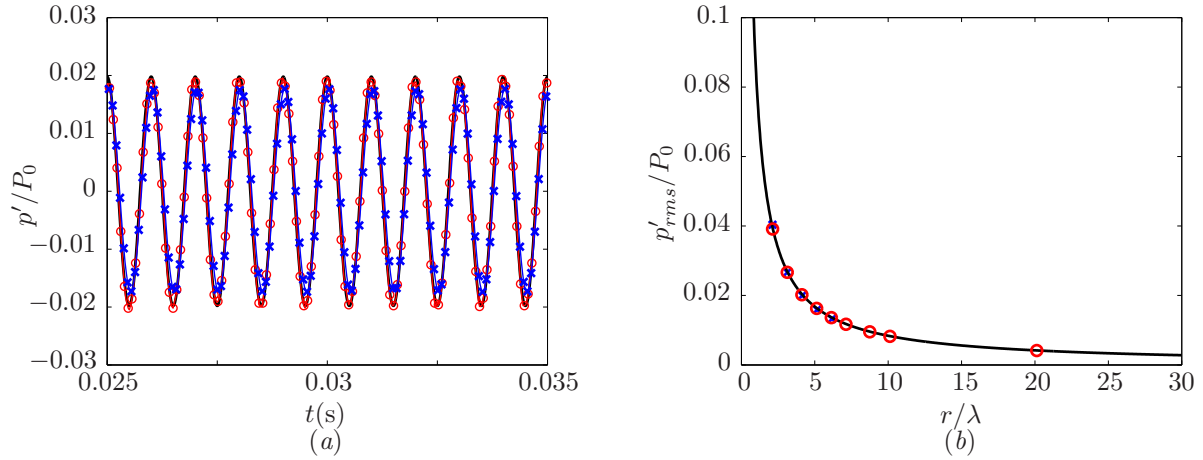
Figure 1. Comparison between theoretical value (———), direct LBM simulation (×), and FW-H calculation (○); (*a*) Acoustic pressure time history at $r = 6\lambda$; (*b*) RMS value of the acoustic pressure as a function of the propagation distance from the source.

Figure 1(*a*) shows the acoustic pressure time history at a distance $r = 6\lambda$ from the source, for the simulation with 20 points per wavelength. The comparison between the theoretical value and the results from the direct LBM simulation and the FW-H calculation shows very good agreement, both in the near-field and far-field. The same conclusion holds for the rms value of the acoustic pressure, shown in figure 1(*b*) as a function of the distance from the source. As expected, the theoretical decay proportional to the propagation distance is observed. It can also be verified that the directivity pattern is omni directional, for both the direct LBM simulation and the FW-H calculation. This results confirms that the acoustic waves are accurately predicted even when the direction of propagation is not aligned with the mesh.

To investigate the effect of FW-H input surface shape and position (at a given resolution), the near-field data is recorded on additional surfaces enclosing the monopole: a cube of size 2λ centered at the origin, and an off-centered cylinder of radius λ and side 1.5λ. In particular, the cylinder position was chosen such that it intersects a resolution transition, to quantify the influence of the grid. The variation in RMS pressure between the different input surfaces was less than 1 %, for every microphone position. For this simple case, the results indicate that the far-field prediction is largely independent of the input surface shape and position. Likewise, there is no noticeable detrimental effect of using input surface crossing different resolution regions. Further analysis would be required to extend these conclusions to more complex cases.

The monopole case in a fluid at rest also had the particularity that it can be solved with both formulation 1A and GT ($M_0 = 0$). As expected, both methods yield identical results. For this simple validation study, the different FW-H input files are very small (a few thousand panels and time frames), and only a few observers are considered. Therefore, the calculations are performed in a few seconds and do not show any significant differences in performances between the two formulations. For practical application such as landing noise where both methods are applied (i.e., for fly-over certification and for wind-tunnel testing), the current serial version with formulation GT is in general about 15 to 20% faster than 1A (depending on the number of panels and observers).

IV.   Tandem cylinder noise prediction

A.   Numerical setup

The tandem cylinder configuration is a typical interaction problem commonly encountered in aircrafts, and is one of the subjects of the AIAA Workshop on Benchmark problems for Airframe Noise Computations (BANC-1). A series of experiments have been performed in a closed section wind-tunnel (NASA Basic Aerodynamics Research Tunnel, referred to as BART) and in an open-jet anechoic tunnel (NASA Quiet Flow Facility, referred to as QFF). Both near-field aerodynamic data[28–31] and acoustic radiation measurements[30, 32] were collected.

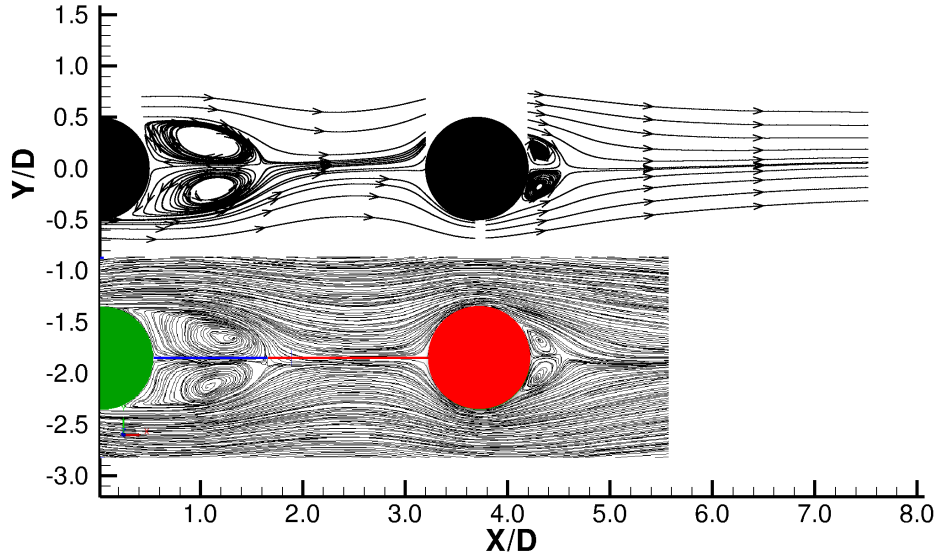American Institute of Aeronautics and Astronautics

Figure 2. Streamlines in the midsection plane $z/D = 0$: PIV measurements (top) and LBM simulation (bottom).

For the benchmark test selected, the identical cylinders of diameter $D = 0.05715$ m are separated by a distance of 3.7 D, and the flow Mach number is $M_0 = 0.128$, corresponding to a freestream velocity $U_0 = 44$ m/s. The resulting Reynolds number is $Re = U_0 D/\nu = 166000$. The cylinder span is 12.4 D in the closed wind-tunnel, and 16 D in the open-jet anechoic wind-tunnel.

The numerical simulation performed with the LBM code matches the experimental setup, and the extent of the computation domain is 16 D, with periodic boundary conditions in the spanwise direction. The resolution is primarily concentrated near the cylinders, with 128 cells per diameter at the surface of both cylinders, corresponding to a finest cell size of 0.446 mm. The total simulated time is 0.5 s and the temporal convergence is achieved after approximately 0.1 s. Additional details on the experimental and numerical setups, as well as complete comparison of the aerodynamic results are presented in Ref. 33. As the focus of the present work is to demonstrate and validate the far-field noise capability, only a few representative aerodynamic results are discussed here.

B. Representative near-field results

Figure 4 shows the comparison of the PIV measurements[34] with the mean flow structures between the cylinders from the LBM simulation, in the mid-section plane $z/D = 0$. The results indicate that both the shape and the length of the wakes are accurately predicted by simulation. In the experiment, the separation point is located at $\theta \approx 110°$ on the upstream cylinder and $\theta \approx 130°$ on the downstream cylinder. As shown in figure 4, these values are predicted accurately in the simulation ($\theta \approx 109°$ and $\theta \approx 138°$, respectively).

As mentioned in section IID, accurate results for the pressure on the surface are critical for the far-field noise predictions in *wind-tunnel* cases using solid integration surfaces. The mean coefficient of pressure $C_P = (\bar{P} - P_0)/1/2\rho_0 U_0^2$ on the surface of both cylinders is presented in figure 3(a) and (b), as a function of the angle θ (measured from the upstream stagnation point). The simulation data is averaged in the spanwise direction. There is an excellent agreement between the simulation and the experiment, in particular with the QFF data.

Likewise, the pressure fluctuations on both cylinders are well predicted in the simulation, as shown in figure 4. On the downstream cylinder at $\theta = 45°$ (figure 4(b)), the agreement between the three data sets is nearly perfect. Even the small peaks at approximately 350 Hz, 550 Hz and 700 Hz are captured in the simulation. This measurement location corresponds to a region of strong interaction between the front wake and the downstream cylinder, leading to much higher dB levels than on the upstream cylinder. The primary shedding frequency in the simulation is $f \approx 179$ Hz, matching the measured shedding frequency of 178180 Hz from the experiments.
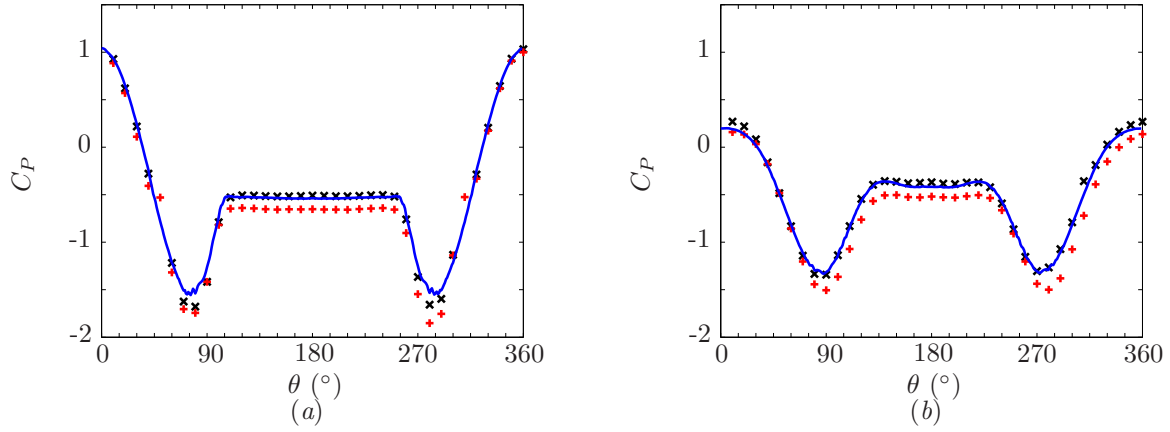
American Institute of Aeronautics and Astronautics

Figure 3. Mean coefficient of the surface pressure for BART (+) and QFF (×) experiments, and LBM simulation (——): (*a*) upstream cylinder; (*b*) downstream cylinder.

On the upstream cylinder at $\theta = 135°$ (figure 4(*a*)), excellent agreement is again observed up to 500 Hz, with both the primary shedding frequency and the first harmonic accurately predicted. Above that frequency, there are significant differences between the three data sets. The pressure fluctuation levels in the experimental measurements tend to flatten out and remain constant around 90 dB (with the BART data about 3 to 5 dB lower) up to 1500 Hz, and then decay again at a constant rate. This particular shape of the spectra could potentially be caused by the boundary layer trip in the experiment. In contrast, there is no trip in the simulation and no change in slope in the spectra for the numerical results. The decay rate over these frequencies tends to match the value from the QFF data above 1500 Hz. Additionally, a peak of approximately 8 dB is predicted around 1000 Hz, which is not observed in the experiments. This peak might be related to the surface roughness used in the simulation. Here, this particular measurement location is past the separation point of the upstream cylinder and experiences much smaller pressure fluctuations than the downstream cylinder.
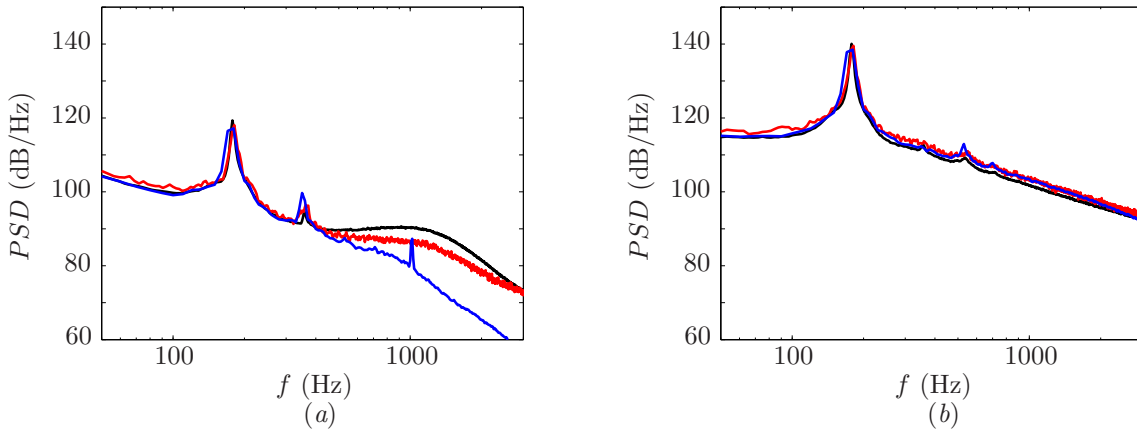

Figure 4. Surface pressure spectra for BART (——) and QFF (——) experiments, and LBM simulation (——): (*a*) upstream cylinder at $\theta = 135°$; (*b*) downstream cylinder at $\theta = 45°$.

Additional work and further analysis are required to investigate these discrepancies and explain the presence of the peak at 1000 Hz in the simulation. Nevertheless, these results demonstrate that the mean and unsteady pressure on both cylinders is accurately predicted in the LBM computation. Since the differences occur at higher frequencies, and much smaller levels, it is not expected to significantly affect the radiated noise.

American Institute of Aeronautics and Astronautics

C. Far-field results

In the open-jet anechoic wind-tunnel, the radiated noise was measured at three microphones, within the mid-span plan above the cylinders. Microphone A is at $(-8.33D, 27.815D)$, microphone B at $(9.11D, 32.49D)$, and microphone C at $(26.55D, 27.815D)$. Shear-layer correction was not applied.

This case is representative of the *wind-tunnel* capability, and the acoustic analogy method is used to predict the noise at the same locations. For the results presented here, only the pressure fluctuations on the solid surface of both cylinders are used as input to the FW-H solver (i.e., solid surface formulation). In future work, additional CFD measurements in the cylinder near-field will be recorded to enable the use of the porous surface formulation.

The length of the time signal used as input for the far-field solver corresponds to the last 0.3 s of the simulation, which is more than 50 periods of the primary shedding frequency. The FW-H input measurement has a sampling rate of approximately 20 kHz, and contains about 1.5 million panels. The power spectra density (PSD) in dB/Hz (rel. to 20 10^{-6} Pa) is computed using hanning window (50% overlap), and samples of 10 Hz bandwidth.

Figures 5(a), (b) and (c) show the spectra of the radiated noise at the microphone A, B and C, respectively. Good agreement is obtained between the far-field solver predictions and the QFF measurements, for both the shape of the spectra and the overall levels. Similarly, the frequency of the tonal peak generated by the periodic shedding, as well as the first harmonics, is accurately predicted.
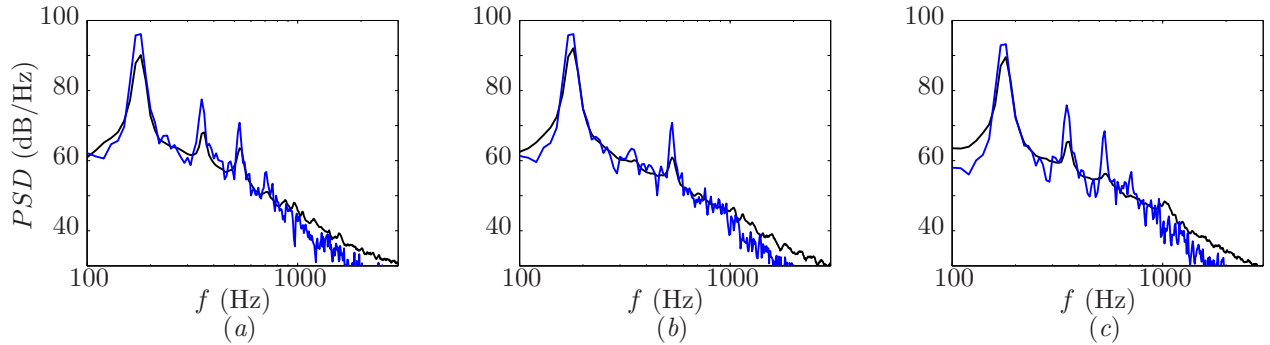

Figure 5. Power spectral density of the radiated noise for the QFF experiment (———) and the FW-H solver (———): (a) at microphone A; (b) at microphone B; (c) at microphone C.

However the predicted peak levels are systematically higher. This can be expected because of the periodic boundary conditions used in the simulation, compare to solid end walls in the experiments. In figure 5, the full span of 16D was used as input to the FW-H solver. In the BART and QFF experiments, the spanwise coherence at the shedding frequency is estimated around 4 to 6D. Similar results are reported for the spanwise correlation. Therefore, using only a reduced span of 8D as input to the FW-H solver, the predicted peak levels can be shown to drop and match the levels in the QFF experiments.[33] However, the overall levels tend to drop as well and the noise is slightly under predicted in this case.

D. Preliminary results for QFF simulations

Overall, the comparison of the far-field results show good agreement, but suggest that the solid walls present in the spanwise direction in the experiment should be included in the simulation, to obtain better correlation.

In order to address this issue and investigate installation effects, an additional configuration matching the QFF setup and geometry (including the open jet and the solid end plates in the span) is considered.[33] The flow conditions, resolution, and measurement parameters are unchanged. Details on the numerical setup and simulation will be presented in future publications. Only 0.2 s of physical time was simulated at this stage, with the temporal convergence approximately achieved again around 0.1 s. Therefore, the length of the time signal used as input to the FW-H solver corresponds to the last 0.1 s of the simulation, and the power spectra density is now computed for samples of 20 Hz bandwidth.

The comparison between the QFF experiment and the FW-H results (for the QFF setup) is shown in figure 6. Given the very short time signal used for the far-field prediction, these preliminary results are very
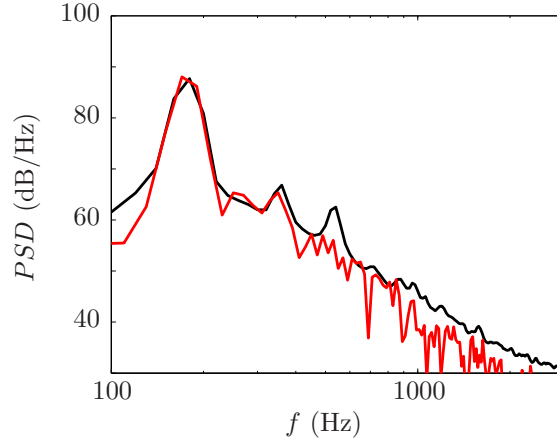
American Institute of Aeronautics and Astronautics

Figure 6. Power spectral density of the radiated noise at microphone A for the QFF experiment (————) and the FW-H solver (————) for the LBM simulation matching the QFF geometry. Note that only 0.1 s of data was available for the FW-H prediction at this stage.

encouraging. Here, the full span of the solid surface of both cylinders is again used as input to the FW-H solver. However, unlike the results with periodic boundary conditions in figure 5, the dB levels at the main peak frequency and the first harmonic are now well predicted. Likewise, the overall levels and shape of the spectra are well captured. A longer time signal and therefore better statistical averaging can be expected to improve the predictions in the low frequency and smooth out the dB levels. Further analysis, including comparisons with the experimental measurements for the mean and unsteady near-field, will be presented in future publications.

V. Preliminary results for fan noise

The last case corresponds to a six-blade fan moving in a fluid at rest, with the fan rotation truly reproduced at the physical angular velocity. Since typical measurements are performed in relatively close proximity to the fan, the noise can be computed directly in the LBM simulation, and the acoustic analogy is not required for practical use. Here, the results from the FW-H solver are only shown as an example to demonstrate the *moving-source* capability of the far-field noise prediction code.

For simulations of flow with arbitrary geometry rotating in time around a fixed axis, the three dimensional computational domain is divided into an inner and outer region. The inner region has a grid attached to the rotating geometry so that the geometry does not have a relative motion with respect to the grid. This forms a "body-fixed" Local Reference Frame (LRF) domain with the rotating geometry. The grid in the outer region is stationary and forms a "ground-fixed" reference frame domain. Between the inner domain and outer domain, there is a closed transparent interface connecting the fluid regions.[35–38]

A. Numerical setup

The fan geometry (including the rotation axis) and a schematic of the numerical setup near the fan is presented in figure 7. The overall simulation setup is similar to the configuration in Ref. 38, where the fan is enclosed in a solid wall shroud which extends to the boundary of the simulation domain (not represented in figure 7). The fan is centered at $(x_0, y_0, z_0) = (0, 0, 0)$ above the bottom wall $z = -1$ m. The microphone is located at $x = -1$ m in front of the blades center, on the axis of rotation. The diameter of the fan and of the hub is 437 mm and 151 mm, respectively. The rotation speed is fixed to 2500 rpm and the tip velocity is 57.2 m/s.

A total of 1 s of physical time is simulated, corresponding to about 42 complete fan rotations. The initial condition is the fluid at rest, and the flow and noise convergence is obtained after approximately 7 rotations. Figure 8(*a*) shows the streamlines and mean velocity magnitude in midsection plane (y=0), and the details of the grid resolution near the blades. Here, the streamlines clearly show the influence of the bottom wall

American Institute of Aeronautics and Astronautics

on the flow field. The resolution close to the blade surfaces and in the shroud area is 1.0 mm, corresponding to 437 points per fan diameter, and the total number of cells is about 24.5 million. The time step based on the finest resolution is 1.65 10^{-6} s, and for 1 s of simulation time, the computational cost is approximately 10 kCPU hours.
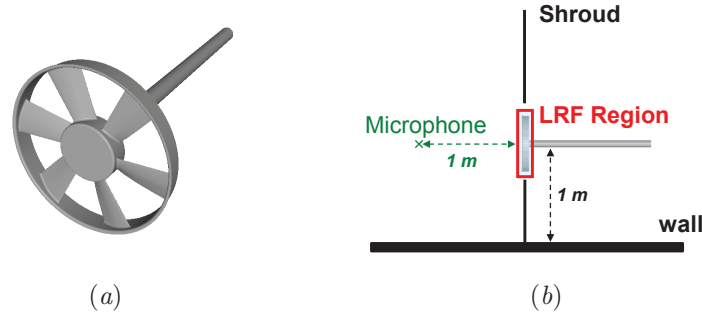

Figure 7. Simulation details: (a) fan geometry; (b) schematic of the numerical setup (not to scale). Only the region near the fan is shown (i.e., the solid wall shroud extends to the edge of the simulation domain).
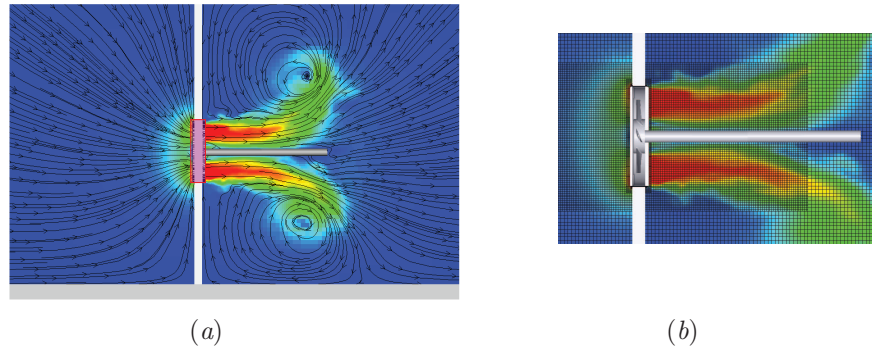

Figure 8. Mean flow field in midsection plane: (a) streamlines and velocity magnitude; (b) zoomed in view with details of the grid resolution.

The input data for the FW-H solver is the pressure fluctuations from the LBM simulation on the solid surface which coincides with the fan blade geometry. The FW-H measurement file is sampled at approximately 5 kHz, and contains about 0.5 million panels. Additional information about the surface motion is also required for a *moving-source* case, namely here the angular velocity of the blade. For both the FW-H input measurement and the LBM direct propagation measurement, the length of the time signal used corresponds to the last 0.5 s of the simulation.

For the fan noise, the power spectra density is computed in A-weighted dB using again the hanning window (50% overlap), and samples of 10 Hz bandwidth. Figure 9 shows the comparison of the spectra at the microphone for the direct LBM simulation and the initial FW-H calculation (in red). Since the fan rotates at 2500 rpm, the blade passage frequency (BPF) is 250 Hz. The BPF and its harmonic are well captured with both methods. However, the dB levels are underestimated with the FW-H solver compare to the direct propagation, which could seem counter intuitive at first. The anticipated reason for this trend is that the acoustic analogy does not take into account the presence of the solid walls (shroud and bottom wall), while their contribution to the noise is directly resolved and included in the LBM simulation.

To validate this assumption, first, the classical method of images and acoustic reciprocity are used to estimate the reflections from the bottom wall (see Chap. 6 in Ref. 26). The pressure fluctuations at the *image* microphone located at $(-1, 0, -2)$ m (i.e., the symmetric position of the *original* microphone with respect to the rigid planar boundary $z = -1$ m) is computed with the FW-H solver, using the same input source. Then, the pressure histories of both the *original* and *image* microphone are summed in the time domain. The resulting acoustic field now accounts for both the (perfect) reflections on the bottom wall and

the direct noise propagation from the source. Finally, since the fan is mounted on a rigid plane boundary (i.e., *baffle*[26] boundary), the fan is approximated as a baffled incoherent source. The estimated effect of the shroud is therefore to add 3 dB to the noise levels.

Both estimated contributions are taken into account in the final FW-H calculation in figure 9 (black curve). Not only the levels are increased, but the shape of the spectra is also corrected in the low frequencies, and the agreement with the direct propagation in the LBM simulation is now excellent, up to approximately 1000 Hz. Some discrepancies are observed for the higher frequencies mainly because of the current sampling frequency used for the FW-H input measurement. As discussed in section IIIB, the cutoff for an input data sampled at 5 kHz can be expected around 1000 Hz to 1250 Hz, which is what is observed is figure 9. Better agreement in the high frequency can therefore be expected by simply increasing the sampling rate of the FW-H input data. Nevertheless, this results demonstrate that, for the rotating fan, the noise sources in the simulation can be accurately predicted with the far-field solver, and therefore validate the *moving-source* capability.
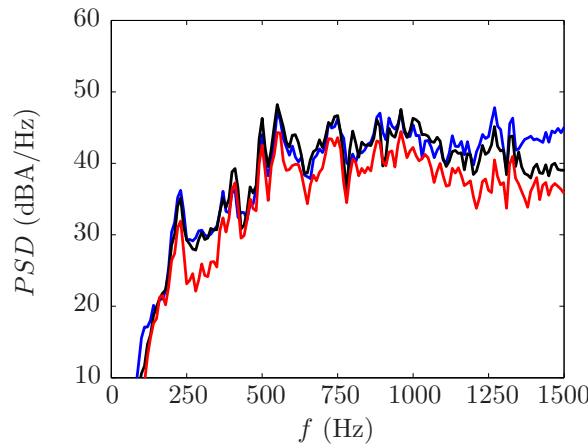

Figure 9. Spectra at 1 m in front of the fan center: direct propagation in LBM simulation (———); FW-H calculation (———); FW-H calculation including wall reflections and shroud effect (———).

VI.   Conclusions

This paper presents the development, implementation and validation of an efficient far-field noise prediction code. This module uses the near-field CFD results from a Lattice-Boltzmann flow solver as input to an acoustic analogy solver based on the Ffowcs Williams–Hawkings equation.

Different FW-H formulations are implemented to efficiently perform far-field prediction from the large data sets provided by the LBM computation. For *moving-source* configurations (i.e., aircraft certification), the efficient and well-validated formulation 1A is implemented. For *wind-tunnel* configurations where both the source and observer are stationary in a uniform flow, a formulation based on the Garrick Triangle, and referred to as GT, is used to increase the computational efficiency. The formulations are implemented in the time domain, using the source-time dominant algorithm. The input to the FW-H solver is the time-dependent flow field on a surface mesh, both provided by CFD simulations with the LBM code. This surface mesh can be defined either as a solid (impenetrable) surface, or porous (permeable) data surface.

Three representative validation cases are considered. First, the coupling between the CFD and the acoustic analogy method is validated with a three-dimensional monopole source study. Then, for tandem cylinder flow (representative of the *wind-tunnel* capability), the predicted noise from simulation is compared to the measured radiated noise from experiment. The results show very good agreement, in particular when the numerical setup in the LBM simulation closely match the experimental setup. Finally, preliminary results for fan noise demonstrated the *moving-source* capability, including the possibility to estimate reflections off rigid planar surfaces and baffled source effects.

As the FW-H formulations and implementation are well suited to handle large sets of time-dependent CFD input, future use of the solver will focus on practical engineering problems such as landing gear noise,

train certification, and wind turbine noise. Additional work and developments include the completion of the parallel version, the implementation of the convective formulation for arbitrary moving source in uniformly moving media, and investigation of the quadrupole term contribution.

Acknowledgments

The authors would like to thank Ali Najafi-Yazdi and Prof. Luc Mongeau, from McGill University, for their significant contributions to the early code development, and Min-Suk Kim, from Exa Corporation, for his help on the fan noise study. The authors are also grateful to Prof. Pierre Sagaut for providing the fan geometry and useful comments.

References

[1] Ffowcs Williams, J. E. and Hawkings, D. L., "Sound generation by turbulence and surfaces in arbitrary motion," *Proc. R. Soc. Lond. A*, Vol. 264, 1969, pp. 321–342.

[2] Li, Y., Shock, R., Shang, R., and Chen, H., "Numerical Study of Flow Past an Impulsively Started Cylinder by the Lattice-Boltzmann Method," *J. Fluid Mech.*, Vol. 519, 2004, pp. 273–300.

[3] Fares, E., "Unsteady Flow Simulation of the Ahmed Reference Body using a Lattice Boltzmann Approach," *Comput. Fluids*, Vol. 35(8-9), 2006, pp. 940–950.

[4] Ricot, D., Maillard, V., and Bailly, C., "Numerical Simulation of the Unsteady Flow Past a Cavity and Application to Sunroof Buffeting," AIAA Paper 2001-2112, 2001.

[5] Adam, J.-L., Ricot, D., Dubief, F., and Guy, C., "Aeroacoustic simulation of automobile ventilation outlets," JASA vol. 123, issue 5, p. 3250, 2008.

[6] Keating, A., Beedy, J., and Shock, R., "Lattice Boltzmann Simulations of the DLR-F4, DLR-F6 and Variants," AIAA Paper 2008-749, 2008.

[7] Keating, A., Dethioux, P., Satti, R., Noelting, S., Louis, J., Van de Ven, T., and Vieito, R., "Computational Aeroacoustics Validation and Analysis of a Nose Landing Gear," AIAA Paper 2009-3154, 2009.

[8] Vaillant, O. and Maillard, V., "Numerical Simulation of Wall Pressure Fluctuation on a Simplified Vehicle Shape," AIAA Paper 2003-3271, 2003.

[9] Pérot, F., Meskine, M., and Vergne, S., "Investigation of the Statistical Properties of Pressure Loadings on Real Automotive Side Glasses," AIAA Paper 2009-3402, 2009.

[10] Chen, H., Teixeira, C., and Molvig, K., "Digital Physics Approach to Computational Fluid Dynamics, Some Basic Theoretical Features," *Intl. J. Mod. phys. C*, Vol. 8(4), 1997, pp. 675.

[11] Chen, S. and Doolen, G., "Lattice Boltzmann Method for Fluid Flows," *Ann. Rev. Fluid Mech.*, Vol. 30, 1998, pp. 329–364.

[12] Shan, X., Yuan, X., and Chen, H., "Kinetic Theory Representation of Hydrodynamics: a way beyond the Navier–Stokes equation," *J. Fluid Mech.*, Vol. 550, 2006, pp. 413–441.

[13] Kotapati, R., Keating, A., Kandasamy, S., Duncan, B., Shock, R., and Chen, H., "The Lattice-Boltzmann-VLES Method for Automotive Fluid Dynamics Simulation, a Review," SAE Paper 2009-26-057, 2009.

[14] Farassat, F. and Succi, G. P., "The Prediction of Helicopter Discrete Frequency Noise," *Vertica—*, Vol. 7(4), 1983, pp. 309–320.

[15] Brentner, K. S. and Farassat, F., "An analytical comparison of the acoustic analogy and Kirchhoff formulations for moving surfaces," *AIAA J.*, Vol. 36, 1998, pp. 1379–1386.

[16] Najafi-Yazdi, A., Brès, G. A., and Mongeau, L., "An Acoustic Analogy Formulation for Moving Sources in Uniformly Moving Media," *Proc. Royal Soc. Lond. A*, 2010, in press.

[17] Garrick, I. E. and Watkins, E. W., "A Theoretical Study of the Effect of Forward speed on the Free Space Sound Pressure Field Around Helicopters," Tech. Rep. TR-1198, NACA, 1954.

[18] Lockard, D. P., "A Comparison of Ffowcs Williams – Hawkings Solvers for Airframe Noise Applications," AIAA Paper 2002-2580, 2002.

[19] Farassat, F., "Derivation of Formulations 1 and 1A of Farassat," Tech. Rep. TM-2007-214853, NASA, 2007.

[20] Brentner, K. S. and Farassat, F., "Modeling aerodynamically generated sound of helicopter rotors," *Prog. Aerospace Sci.*, Vol. 39, 2003, pp. 83–120.

[21] Wells, V. L. and Y., H. A., "Acoustics of a Moving Source in a Moving Medium with Application to Propeller Noise," *J. Sound Vib.*, Vol. 184(4), 1995, pp. 651–663.

[22] Najafi-Yazdi, A., Mongeau, L., and Brès, G. A., "An Acoustic Analogy Formulation for Uniformly Moving Media: Formulation 1C," AIAA paper 2010-3706, 2010.

[23] Brès, G. A., Brentner, K. S., Perez, G., and Jones, H. E., "Maneuvering rotorcraft noise prediction," *J. Sound Vib.*, Vol. 275, 2004, pp. 719–738.

[24] Casalino, D., "An advanced time approach for acoustic analogy predictions," *J. Sound Vib.*, Vol. 261, 2003, pp. 583–612.

[25] Noelting, S., Brès, G. A., Dethioux, P., Van de Ven, T., and Vieito, R., "A Hybrid Lattice-Boltzmann/FH-W Method to Predict Sources and Propagation of Landing Gear Noise," AIAA Paper 2010-3976, 2010.

[26] Kinsler, L. E., Frey, A. R., Coppens, A. B., and Sanders, J. V., *Fundamentals of acoustics*, John Wiley & Sons Inc., New York, 4th ed., 2000.

[27]Brès, G. A., Pérot, F., and Freed, D., "Properties of the Lattice–Boltzmann Method for Acoustics," AIAA Paper 2009-3395, 2009.

[28]Jenkins, L. N., Khorrami, M. R., Choudhari, M. M., and McGinley, C. B., "Characterization of unsteady flow structures around tandem cylinders for component interaction studies in airframe noise," AIAA paper 2005-2812, 2005.

[29]Jenkins, L. N., Neuhart, D. H., McGinley, C. B., Choudhari, M. M., and Khorrami, M. R., "Measurements of unsteady wake interference between tandem cylinders," AIAA paper 2006-3202, 2006.

[30]Lockard, D. P., Khorrami, M. R., Choudhari, M. M., Hutcheson, F. V., Brooks, T. F., and Stead, D. J., "Tandem cylinder noise predictions," AIAA paper 2007-3450, 2007.

[31]Neuhart, D. H., Jenkins, L. N., Choudhari, M. M., and Khorrami, M. R., "Measurements of the flowfield interaction between tandem cylinders," AIAA paper 2009-3275, 2009.

[32]Hutcheson, F. V. and Brooks, T. F., "Noise radiation from single and multiple rod configurations," AIAA paper 2006-2629, 2006.

[33]Brès, G. A., Wessels, M., and Noelting, S., "Tandem Cylinder Noise Predictions Using Lattice Boltzmann and Ffowcs Williams – Hawkings Methods," AIAA Paper 2010-3791, 2010.

[34]Khorrami, M. R., Choudhari, M. M., Lockard, D. P., Jenkins, L. N., and McGinley, C. B., "Unsteady Flowfield Around Tandem Cylinders as Prototype Component Interaction in Airframe Noise," *AIAA J.*, Vol. 45(8), 2007, pp. 1930–1941.

[35]Guo, Z., Zhen, C., and Shi, B., "Discrete lattice effects on the forcing term in the lattice Boltzmann method," *Phys. Rev. E*, Vol. 65(4), 2002, pp. 046308.

[36]Zhang, R., Shan, X., and Chen, H., "Efficient Kinetic Method for fluid simulation beyond Navier-Stokes equation," *Phys. Rev. E*, Vol. 74(4), 2006, pp. 046703.

[37]Pérot, F., Moreau, S., Kim, M. S., and Neal, D., "Investigation of the Flow Generated by an Axial 3-Blade Fan," 13th ISROMAC 2010-082, 2010.

[38]Pérot, F., Kim, M. S., Moreau, S., Henner, M., and Neal, D., "Direct aeroacoustics prediction of a low speed axial fan," AIAA paper 2010-3887, 2010.